Monthly Notices
of the
ROYAL ASTRONOMICAL SOCIETY

MNRAS **496,** 3741–3754 (2020) doi:10.1093/mnras/staa1775

Structural parameters for the globular-cluster-like objects in NGC 1052-DF2

Jun Ma,[1,2]★ Shoucheng Wang,[1,2] Song Wang,[1] Zhimin Zhou,[1]★ Tianmeng Zhang,[1,2] Jundan Nie,[1] Hu Zou,[1] Xu Zhou,[1] Cuihua Du,[2] Jiali Wang[1] and Jianghua Wu[3]

[1]*CAS Key Laboratory of Optical Astronomy, National Astronomical Observatories, Chinese Academy of Sciences, Beijing 100101, China*
[2]*College of Astronomy and Space Sciences, University of Chinese Academy of Sciences, Beijing 100049, China*
[3]*Department of Astronomy, Beijing Normal University, Beijing 100875, China*

Accepted 2020 June 12. Received 2020 June 12; in original form 2019 November 21

ABSTRACT

Recently, van Dokkum et al. have found an ultra-diffuse galaxy NGC 1052-DF2 with little or no dark matter, based on a spectroscopic study of its 11 constituent globular-cluster-like objects. In this paper, we analyse these 11 objects using *Hubble Space Telescope* imaging. We derive the structural parameters for each object by fitting the surface brightness profiles to three different models. Our results indicate that these objects are better fitted by the Wilson model than by the King and Sérsic models. Using the distance of $D = 20$ Mpc to NGC 1052-DF2 obtained by van Dokkum et al., these 11 objects have half-light radii in the range from ∼11 to ∼16 pc. These values are much larger than for normal globular clusters in the Milky Way, and are comparable to the sizes of an extended star cluster and of a typical ultra-compact dwarf. The half-light radii obtained here are larger than those obtained by van Dokkum et al. and Trujillo et al. The offset of the differences between the half-light radii of van Dokkum et al. and ours is 6.17 pc, and the offset of the differences between the half-light radii of Trujillo et al. and ours is 4.99 pc. Our half-light radii are, on average, 11.74 pc, which corresponds to 53 and 43 per cent larger than those obtained by van Dokkum et al. and Trujillo et al., respectively. The $R_{\rm h}$ versus M_V diagram shows that these objects occupy the same areas of extended star clusters and ultra-compact dwarfs. Using the distance of $D = 13$ Mpc obtained by Trujillo et al., there are still five objects that do not lie in the area of normal globular clusters in the Milky Way. So, we suggest that these globular-cluster-like objects in NGC 1052-DF2 are not normal globular clusters like those in the Milky Way.

Key words: galaxies: evolution – galaxies: star clusters: general – galaxies: star clusters: individual: NGC 1052-DF2.

1 INTRODUCTION

Ultra-diffuse galaxies (UDGs) are a particular type of low-surface brightness galaxies with a central surface brightness $\mu_{\rm g}(0) >$ 24 mag arcsec^{-2} and an effective radius of $R_{\rm eff} > 1.5$ kpc, and were first discovered in the Coma cluster by van Dokkum et al. (2015a,b). Since the work of van Dokkum et al. (2015a,b), more UDGs in different environments, from dense to sparse, have been discovered (see He et al. 2019; Liao et al. 2019; Lee et al. 2020; and references therein). The formation mechanisms of UDGs are still unclear. Three possible origins have been proposed. (i) van Dokkum et al. (2015a, 2016) and Toloba et al. (2018) have suggested that UDGs are so-called 'failed galaxies' (i.e. UDGs failed to form a typical amount of stars with dark matter halo masses of $\sim 10^{12}$ M$_\odot$ due to some physical process). (ii) Some authors (see Amorisco & Loeb 2016; Chan et al. 2018; Spekkens & Karunakaran 2018; and references therein) have proposed that UDGs are 'extended dwarf galaxies' (i.e. UDGs were extended from normal dwarf galaxies due to their spins or feedback outflows). (iii) UDGs are tidal galaxies – that is,. UDG progenitors were extended by tidal stripping of dwarf galaxies within clusters (see Carleton et al. 2019, and references therein). There is still no consensus regarding the formation of UDGs and, in fact, there are hints that UDGs may have mixed formation mechanisms (see Lim et al. 2018; Pandya et al. 2018; and references therein). NGC 1052-DF2, which was characterized by Fosbury et al. (1978) and Karachentsev et al. (2000), is an UDG with an effective radius of $R_{\rm eff} = 2.2$ kpc and a central surface brightness $\mu(V_{606}, 0) = 24.4$ mag arcsec^{-2} (van Dokkum et al. 2018c). It has recently been the subject of heated debate after

★ E-mail: majun@nao.cas.cn (JM); zmzhou@nao.cas.cn (ZZ)

van Dokkum et al. (2018c) claimed to have detected little or no dark matter for this UDG, based on a spectroscopic study of its constituent globular-cluster-like objects. Then, van Dokkum et al. (2018a) studied these objects using a combination of *Hubble Space Telescope* (*HST*) imaging and Keck spectroscopy. In particular, van Dokkum et al. (2018a) determined the half-light radii $R_{\rm h}$ of these objects by fitting King (1962) models to the surface brightness profiles using the two-dimensional fitting algorithm (GALFIT) with synthetic point spread functions (PSFs), which was developed by Peng et al. (2002) to extract structural components from galaxy images. In addition, van Dokkum et al. (2018c) have assumed that NGC 1052-DF2 is a satellite of the luminous elliptical galaxy NGC 1052 at ≈20 Mpc, on the basis of its projected position (it is located only 14 arcmin away from NGC 1052), its surface brightness fluctuation (SBF) distance of 19.0 ± 1.7 Mpc, and its radial velocity of ≈1800 km s^{-1}. Assuming a distance of $D = 20$ Mpc, van Dokkum et al. (2018c) found the peak of the absolute magnitudes of globular-cluster-like objects in NGC 1052-DF2 to be at $M_{V,\,606} = -9.1$ mag, significantly brighter than the canonical value for globular clusters (GCs) of $M_V \sim -7.5$ mag (Rejkuba 2012; Amorisco, Monachesi & White 2018). Intriguingly, van Dokkum et al. (2018c) showed that, in terms of their sizes and luminosities, these objects are very similar to ω Centauri, which is suggested to be the core of a former dwarf galaxy (see Mackey & van den Bergh 2005, and references therein). However, as pointed out by Trujillo et al. (2019), both the absence of dark matter and the anomalous bright population of globular-cluster-like objects in NGC 1052-DF2 depend critically on the adopted distance of 20 Mpc from association with NGC 1052. There is an ongoing debate regarding the correct distance to NGC 1052-DF2. In an independent SBF analysis, Blakeslee & Cantiello (2018) determined $D = 20.4 \pm 2.0$ Mpc, which is consistent with that in van Dokkum et al. (2018c). However, Trujillo et al. (2019) derived a significantly shorter distance of 13.1 ± 0.8 Mpc using the tip of the red giant branch (TRGB) in NGC 1052-DF2. In response, van Dokkum et al. (2018b) showed that the corresponding colour–magnitude diagram (CMD) is strongly influenced by blends, which can lead to an erroneous TRGB distance ∼1.4 times shorter than the correct distance. At the same time, van Dokkum et al. (2018b) determined $D = 18.7 \pm 1.7$ Mpc using a megamaser–TRGB–SBF distance ladder, which is consistent with van Dokkum et al. (2018c).

An ultra-compact dwarf (UCD) is a compact stellar system, which is more luminous and larger than a typical GC, but more compact than a typical dwarf galaxy. UCDs were originally discovered independently by Hilker, Infante & Richtler (1999) and Drinkwater et al. (2000) in spectroscopic surveys of the centre of the Fornax cluster. UCDs have sizes of $10 < R_{\rm h} < 100$ pc and luminosities of $M_V < -9$ mag (Liu et al. 2015). Until now, there has been ongoing debate about the origin of UCDs (see Ma et al. 2017, and references therein).

It is important to study the spatial structures and dynamics of star clusters, as these characteristics reflect their formation conditions and dynamical evolution within the tidal fields of their galaxies (Barmby et al. 2007). The structural and dynamical parameters of clusters are often obtained by fitting the surface brightness profiles to a number of different models and by using mass-to-light ratios (M/L values) derived from velocity dispersions or population-synthesis models. Since the pioneer work of McLaughlin et al. (2008), three models are often used in the fits. The first is based on a single-mass, isotropic, modified isothermal sphere developed by Michie (1963) and King (1966). The second is a further modification of a single-mass, isotropic isothermal sphere, based on a model originally introduced by Wilson (1975) for elliptical galaxies. The third model is based on the $R^{1/n}$ surface density profile of Sérsic (1968). Using the three models, some authors have achieved some success in deriving structural and dynamical parameters of clusters in the Local galaxies: the Milky Way, the Large and Small Magellanic Clouds, the Fornax and Sagittarius dwarf spheroidal galaxies (McLaughlin & van der Marel 2005), M31 (Barmby et al. 2007, 2009; Wang & Ma 2013), NGC 5128 (McLaughlin et al. 2008), M33 (Ma 2015) and the M81 group (Ma et al. 2017).

As mentioned above, van Dokkum et al. (2018a) only derived the half-light radii $R_{\rm h}$ of the globular-cluster-like objects in NGC 1052-DF2 by fitting King (1962) models. In order to study the properties of these objects for details, we again derive structural parameters of these globular-cluster-like objects in NGC 1052-DF2 by fitting the surface brightness profiles to three models as previous authors have done (see Ma et al. 2017, and references therein). In this paper, we plot the fitted results for every object so that they can be seen clearly. In addition, the results of this paper show that these objects are better fitted by the Wilson (1975) model than by the King (1966) model.

Because some structural parameters of these objects obtained in this paper are distance-dependent quantities, we opt to present results for the distance of $D = 20$ Mpc to NGC 1052-DF2. However, we discuss the properties of these objects using the shorter distance of $D = 13$ Mpc in Section 4.

In this paper, we derive the structural parameters for globular-cluster-like objects in NGC 1052-DF2. We describe the details of the observations and our approach to the data reduction with the *HST* programs in Section 2. We determine the structural parameters of these objects in Section 3. We make comparisons with previous results and discuss these in Section 4. We provide a summary in Section 5.

2 ARCHIVAL IMAGES OF *HST*

The observations used here come from the *HST* program 14644, in which NGC 1052-DF2 was observed by the *HST*/ACS/WFC in the *F*606*W* and *F*814*W* bands. NGC 1052-DF2 was observed with a total exposure time of 2180 s in the *F*606*W* band and 2320 s in the *F*814*W* band on 2016 November 16. We obtained the combined drizzled images from the *Hubble* Legacy Archive. In addition, for easy comparison with catalogues of the GCs in the Milky Way in future work, we transform the ACS/WFC magnitudes in the *F*606*W* and *F*814*W* bands to the standard *V*. Barmby et al. (2007) has presented transformation from ACS/WFC magnitudes to standard *V* magnitudes in their equations (6) and (7) which are used in this paper.

We use these *HST* images to derive the structural parameters of globular-cluster-like objects in NGC 1052-DF2 (see Section 3 for details).

2.1 Ellipticity, position angle and surface brightness profile

The surface photometries of each sample object were obtained from the drizzled images using the STSDAS task, ELLIPSE. First, the centre position of each object was determined using the IMAGES IMCENTROID task. Then, we ran two passes of the ELLIPSE task. In the first pass, we ran it in the usual way (i.e. the ellipticity and position angle were allowed to vary with the isophote semimajor axis) and in the second pass, we forced the isophote ellpticity in the ELLIPSE task to be identically 0 at all radii. Thus, we have circularly

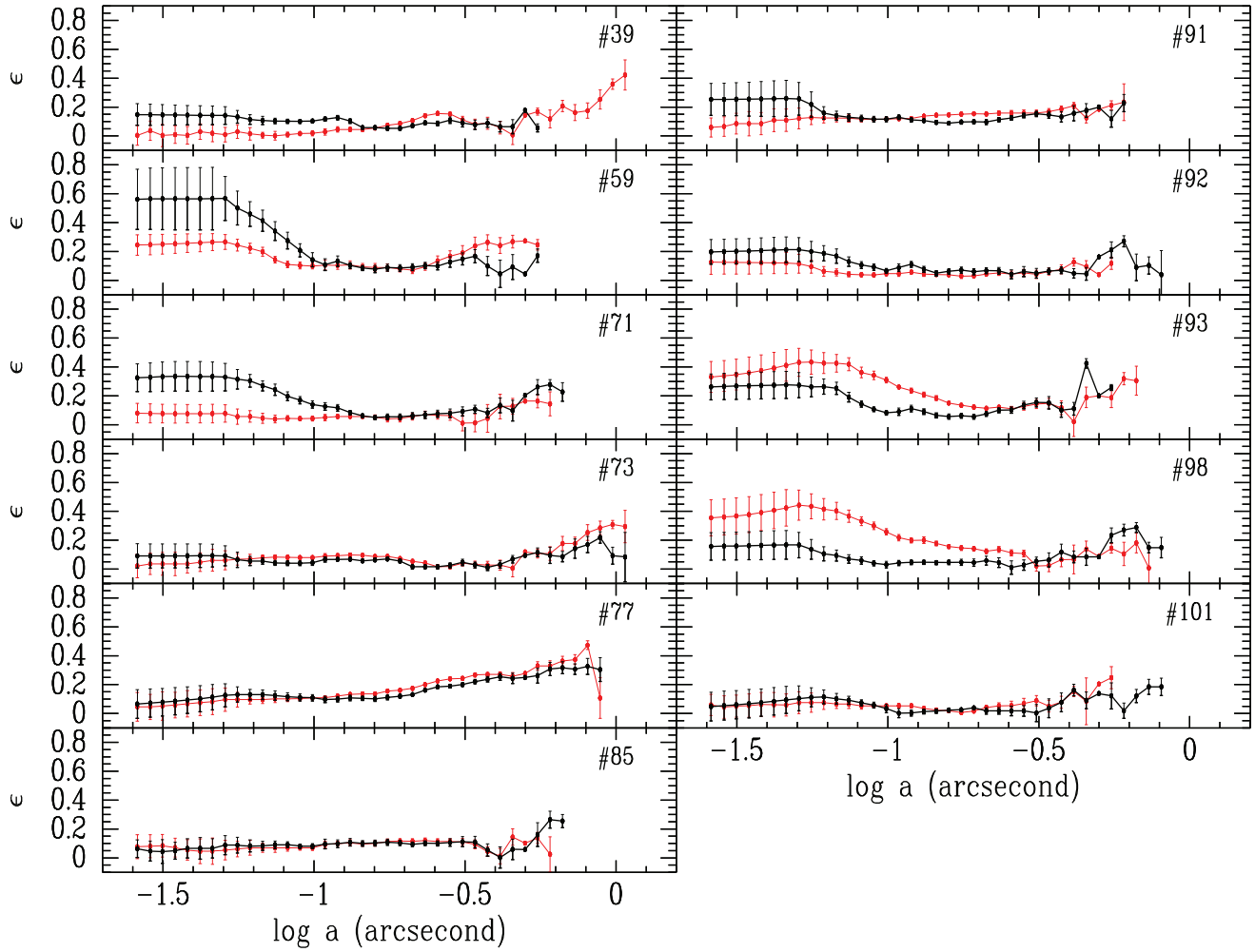

Figure 1. Ellipticity (ϵ) as a function of the semimajor axis (a) in the *F*606*W* (red dots) and *F*814*W* (black dots) filters of *HST*/ACS/WFC for each sample object.

symmetric surface brightness profiles, as we chose to fit circular models for both the intrinsic object structure and the point spread function (PSF) as previous authors have done (see Ma et al. 2017, and references therein). Figs 1 and 2 plot the ellipticity ($\epsilon = 1 - b/a$) and position angle as a function of the semimajor axis length (a) in the *F*606*W* and *F*814*W* bands for these objects. The errors were generated by the ELLIPSE task, in which the ellipticity errors were obtained from the internal errors in the harmonic fit, after removal of the first and second fitted harmonics. Fig. 2 shows that the position angles are occasionally wildly varying, which is likely to be caused by the code. The final ellipticity and position angle for each object were calculated as the average of the values obtained in the first pass of the ELLIPSE task, and are listed in Table 1. Errors correspond to the standard deviation of the mean. Fig. 1 and Table 1 show that the ellipticities of most objects are larger than 0.1, which are larger than the mean value of 0.07 ± 0.01 for the Milky Way GCs (White & Shawl 1987).

As we know, the ELLIPSE task gives the raw output to be in terms of counts s^{-1} $pixel^{-1}$, which must be multiplied by 400 (= 1 pixel $0.05\ arcsec^{-1})^2$ for the ACS/WFC to convert to counts s^{-1} $arcsec^{-2}$. In addition, we transformed the counts to surface brightness in magnitudes calibrated on the VEGAMAG system using equation (1) (from the ACS Handbook):

$$\mu/\mathrm{mag\,arcsec^{-2}} = -2.5\log(\mathrm{counts\,s^{-1}\,arcsec^{-2}}) + \text{zero-point}. \quad (1)$$

In this paper, we worked in terms of linear intensity instead of using surface brightness in magnitudes as previous authors have done (see Ma et al. 2017, and references therein). With updated absolute magnitudes of the Sun, $M_\odot$ (C. Willmer, private communication) listed in Table 2, the equation for transforming counts to surface brightness in intensity can be obtained as

$$I/\mathrm{L_\odot\,pc^{-2}} \simeq \text{conversion factor} \times (\mathrm{counts\,s^{-1}\,arcsec^{-2}}). \quad (2)$$

The zero-points and conversion factors for each filter are listed in Table 2. In this paper, the final, calibrated intensity profiles for these objects with no extinction correction are listed in Table 3, where the points in the last column flagged with 'OK' are used to constrain the model fit, while the points flagged with 'DEP' are those that may lead to excessive weighting of the central regions of objects (for details, see Barmby et al. 2007; McLaughlin et al. 2008). The ELLIPSE task gives isophotal intensities for 15 radii inside $R < 2$ pixels, although all of them are derived from the same innermost 13 pixels. So, the isophotal intensities are not statistically

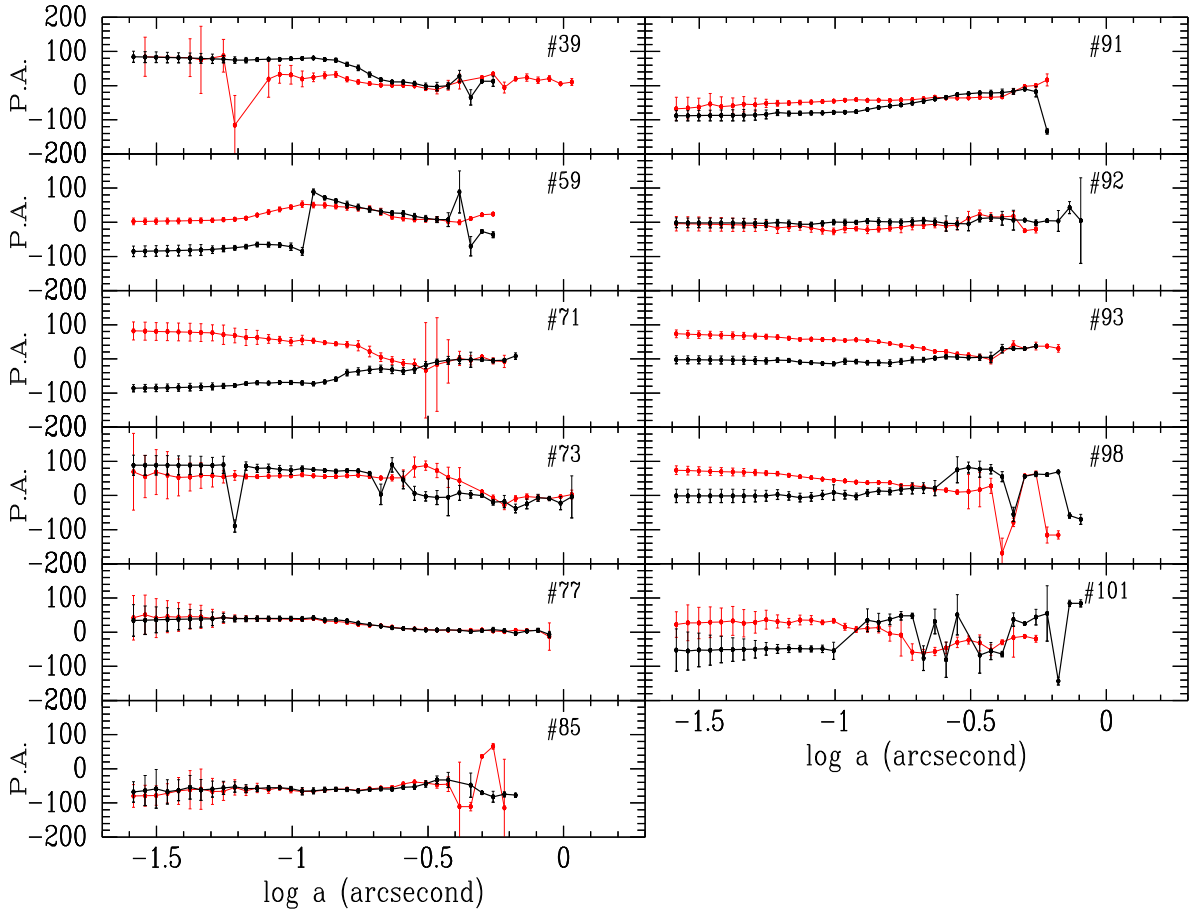

Figure 2. Position angle (P.A.) as a function of the semimajor axis (a) in the *F*606*W* (red dots) and *F*814*W* (black dots) filters of *HST*/ACS/WFC for each sample object.

Table 1. Ellipticity and position angle of the sample objects in NGC 1052-DF2. The object ID in the first column is taken from van Dokkum et al. (2018a). ϵ and θ are the ellipticity and position angle, respectively, of the filters for each cluster, and were obtained in this work.

ID	*F*606*W* filter		*F*814*W* filter	
	ϵ	θ (deg E of N)	ϵ	θ (deg E of N)
39	0.09 ± 0.05	36 ± 1	0.10 ± 0.01	73 ± 7
59	0.18 ± 0.01	42 ± 1	0.26 ± 0.02	-3 ± 2
71	0.07 ± 0.01	59 ± 8	0.19 ± 0.01	-28 ± 10
73	0.09 ± 0.03	65 ± 6	0.07 ± 0.01	62 ± 7
77	0.17 ± 0.01	46 ± 6	0.16 ± 0.02	45 ± 5
85	0.08 ± 0.01	-37 ± 10	0.09 ± 0.03	-38 ± 3
91	0.14 ± 0.02	-20 ± 10	0.16 ± 0.01	-41 ± 12
92	0.07 ± 0.01	13 ± 2	0.12 ± 0.01	23 ± 1
93	0.26 ± 0.01	68 ± 3	0.18 ± 0.01	22 ± 7
98	0.23 ± 0.04	49 ± 25	0.11 ± 0.01	36 ± 14
101	0.07 ± 0.03	23 ± 4	0.07 ± 0.02	1 ± 18

independent. In order to avoid excessive weighting of the central regions of objects in the fits, we only used intensities at radii $R_{\rm min}$, $R_{\rm min}$ +(0.5, 1.0, 2.0) pixels or $R > 2.5$ pixels, as Barmby et al. (2007) used. In addition, points flagged with 'BAD' are those individual isophotes that deviated strongly from their neighbours or showed irregular features, which were not used in constraining the model fit.

Table 2. Calibration data for the ACS/WFC images on the *HST*. The columns are as follows: (1) additive conversion between surface brightness in counts s^{-1} arcsec^{-2} and magnitude in mag arcsec^{-2}; (2) updated absolute magnitude of the Sun (C. Willmer, private communication); (3) multiplicative conversion between surface brightness in counts s^{-1} arcsec^{-2} and intensity in $L_\odot$ pc^{-2}.

Filter	Zero-point (1)	$M_\odot$ (2)	Conversion factor (3)
*F*606*W*	26.398	4.611	0.8207
*F*814*W*	25.501	4.066	1.1349

2.2 Point spread function

The PSF models are critical to accurately measure the shapes of the objects in images taken with *HST* (Rhodes et al. 2006). In this paper, we chose not to deconvolve the data, instead fitting the structural models after convolving them with a simple analytical description of the PSF as previous authors have done (see Ma et al. 2017, and references therein). A simple analytical description of the PSFs for

Table 3. Intensity profiles for the sample objects in NGC 1052-DF2. Note that R is the clustercentric radius. This table is available in its entirety in machine-readable form in the supporting information available online for this paper (table 3.dat).

ID	Filter	R (arcsec)	I ($L_\odot$ pc^{-2})	Uncertainty ($L_\odot$ pc^{-2})	Flag
39	*F606W*	0.0260	632.269	8.368	OK
	F606W	0.0287	617.616	9.321	DEP
	F606W	0.0315	600.018	10.145	DEP
	F606W	0.0347	581.524	10.474	DEP
	F606W	0.0381	564.270	11.538	DEP
	F606W	0.0420	544.482	12.429	DEP
	F606W	0.0461	522.768	13.517	DEP
	F606W	0.0508	499.138	14.250	DEP
	F606W	0.0558	474.406	14.133	OK
	F606W	0.0614	443.231	14.593	DEP
	F606W	0.0676	412.394	13.359	DEP
	F606W	0.0743	377.342	13.024	DEP
	F606W	0.0818	340.127	12.710	OK
	F606W	0.0899	300.318	11.450	DEP
	F606W	0.0989	257.162	11.033	DEP
	F606W	0.1088	217.828	10.086	DEP
	F606W	0.1197	183.980	9.062	DEP
	F606W	0.1317	155.184	7.260	OK
	F606W	0.1448	124.678	5.377	OK
	F606W	0.1593	97.638	4.249	OK
	F606W	0.1752	79.515	3.537	OK
	F606W	0.1928	64.100	3.011	OK
	F606W	0.2120	49.905	2.410	OK
	F606W	0.2333	39.952	1.744	OK
	F606W	0.2566	30.849	1.096	OK

Table 4. Coefficients for the PSF models of the ACS/WFC on the *HST*.

Filter	r_0 (arcsec)	α	β
F606W	0.053	3	3.14
F814W	0.056	3	3.05

the ACS/WFC filters has been given by equation (4) of Wang & Ma (2013), which is used here. We listed the parameters in Table 4.

3 MODEL FITTING

3.1 Structural models

As done by previous authors (see Ma et al. 2017, and references therein), we used three structural models to fit surface profiles of globular-cluster-like objects in NGC 1052-DF2. These three models were presented by King (1966), Wilson (1975) and Sérsic (1968) – hereafter, the King model, Wilson model and Sérsic model, respectively. McLaughlin et al. (2008) have given a detailed description of the three structural models. Here, we briefly summarize some of their basic characteristics.

The King model used here is presented by Michie (1963) and King (1966), which is most commonly used for studies of star clusters. The Wilson model is defined by Wilson (1975), which has more extended envelope structures than the standard King model (for details, see McLaughlin et al. 2008). The Sérsic model has an $R^{1/n}$ surface density profile. Although the Sérsic model is often used for parametrizing the surface brightness profiles of early-type galaxies and bulges of spiral galaxies (Baes & Gentile 2011), Tanvir et al. (2012) have shown that some classical GCs in M31 that exhibit cuspy core profiles are well fitted by the Sérsic model. The clusters with cuspy cores have usually been called post-core collapse (see Noyola & Gebhardt 2006, and references therein).

3.2 Fits

Here, we fit the three models mentioned in Section 3.1 to the brightness profiles of globular-cluster-like objects in NGC 1052-DF2.

We first convolved the three models with PSFs for the filters used. Given a value for the scale radius r_0, we computed a dimensionless model profile $\widetilde{I}_{\rm mod} \equiv I_{\rm mod}/I_0$ and then performed the convolution,

$$\widetilde{I}^*_{\rm mod}(R|r_0) = \int\!\!\int_{-\infty}^{\infty} \widetilde{I}_{\rm mod} \frac{R'}{r_0} \widetilde{I}_{\rm PSF}\left[(x-x'),(y-y')\right]\,{\rm d}x'\,{\rm d}y', \tag{3}$$

where $R^2 = x^2 + y^2$ and $R'^2 = x'^2 + y'^2$. $\widetilde{I}_{\rm PSF}$ is the PSF profile normalized to unit total luminosity (for details, see McLaughlin et al. 2008; Wang & Ma 2013). The best-fitting model was derived by calculating and minimizing χ^2 as the sum of squared differences between model intensities and observed intensities,

$$\chi^2 = \sum_i \frac{[I_{\rm obs}(R_i) - I_0 \widetilde{I}^*_{\rm mod}(R_i|r_0) - I_{\rm bkg}]^2}{\sigma_i^2}, \tag{4}$$

in which a background $I_{\rm bkg}$ was also fitted. The uncertainties of observed intensities listed in Table 3 are used as weights.

We show the fitting for globular-cluster-like objects in NGC 1052-DF2 in Figs 3–13. The observed intensity profile is plotted as a function of logarithmic projected radius. The open squares are the data points used in the model fitting, while the crosses are points flagged as 'DEP' or 'BAD', which were not used to constrain the fit.

3.3 Main model parameters and derived quantities

Table 5 lists the basic and structural parameters of all model fits to globular-cluster-like objects in NGC 1052-DF2, with a simple description of each parameter/column at the end of Table 5. Error bars on all these parameters are defined in the same way as in McLaughlin et al. (2008).

Table 6 lists the 'best-fitting' half-light radii and absolute magnitudes of the sample objects in NGC 1052-DF2.

3.4 Comparison of fits in the *F606W* and *F814W* bands

In this paper, we derived the structural parameters from fitting three different models (King 1966; Wilson 1975; Sérsic 1968) to the radial surface brightness profiles of globular-cluster-like objects in NGC 1052-DF2 in the *F606W* and *F814W* bands. Assessment of the systematic errors and colour dependences in the fits can be done by comparing model fits to the same object observed in different bands (Barmby et al. 2007). Fig. 14 compares the half-light radius ($R_{\rm h}$) derived from fits to the sample objects observed in both the *F606W* and *F814W* bands. In general, the agreement is good except for a few scatters, although the half-light radius from the *F606W* data is a little smaller than that from the *F814W* data for the three models. The offsets of the differences between the *F606W* data and the *F814W* data are −0.722 pc for the King model fits, −0.447 pc for the Sérsic model fits and −0.691 pc for the Wilson model fits. For the M31 star clusters, Barmby et al. (2007) showed that the

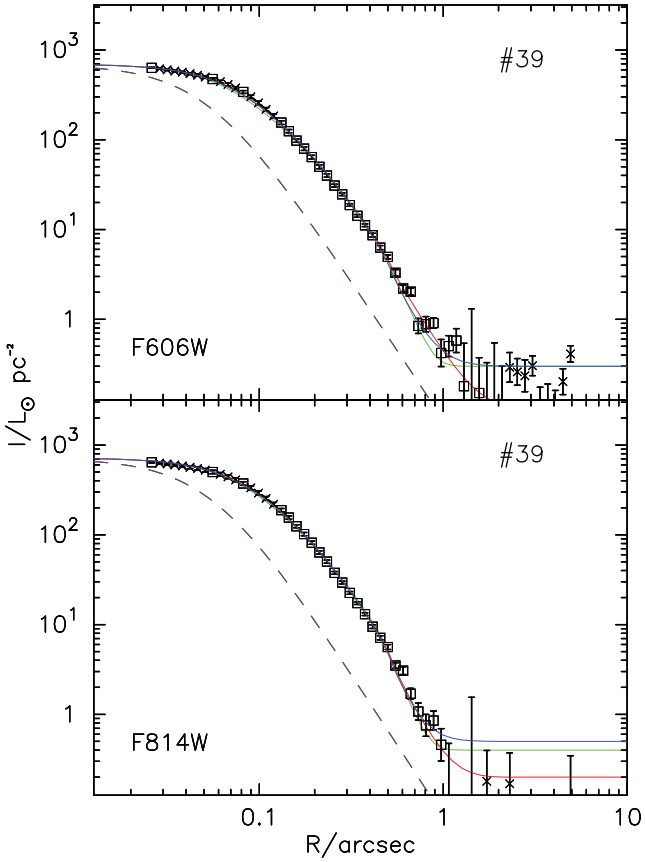

Figure 3. Surface brightness profiles of and model fits to the sample object 39 in NGC 1052-DF2, with the data of *F*606*W* and *F*814*W* bands from top to bottom. The two panels are the fits to the three models. The open squares are the data points used in the model fitting, while the crosses are points flagged as 'DEP' or 'BAD', which are not used to constrain the fit. Solid and dashed curves trace the the PSF-convolved best fits and the PSF intensity profile, respectively: King model (green), Wilson model (red) and Sérsic model (blue).

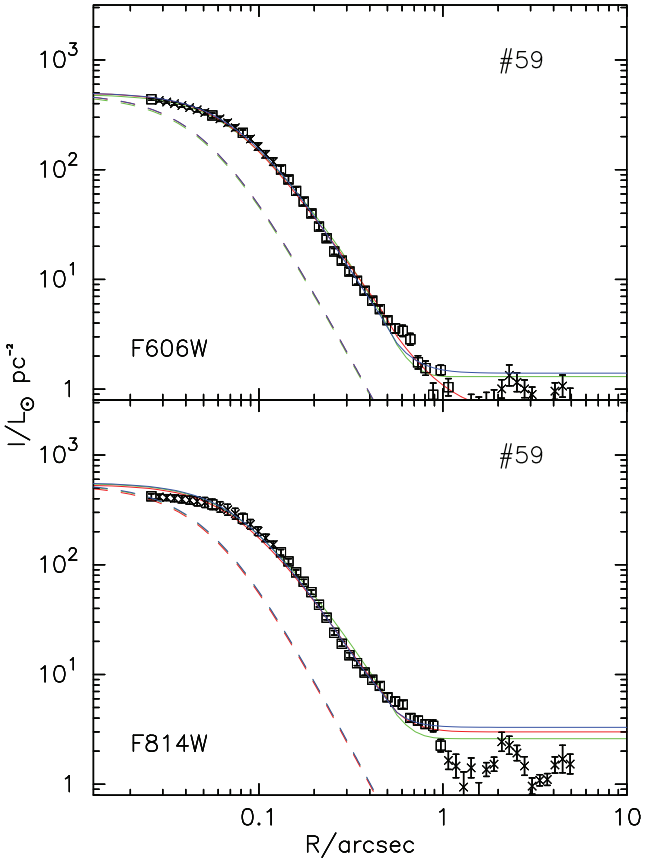

Figure 4. Same as Fig. 3, but with surface brightness profiles of and model fits to the sample object 59 in NGC 1052-DF2.

agreement is better for the King model fits than the Wilson and Sérsic model fits. For the M33 star clusters, Ma (2015) showed that there is larger scatter for the Sérsic and Wilson model fits than for the King model fits.

Because the results of the model fits in the two ACS/WFC bands are similar, we only consider model fits from the *F*606*W* band from now on. In addition, fits to clusters in the Milky Way are performed in the *V* band, allowing us direct comparison without being concerned about possible colour gradients (see Section 4).

3.5 Comparison of three model fittings

In order to present clearly the quality of fit for different models, Fig. 15 shows the relative quality of fit, Δ, for the Wilson and Sérsic model fits (filled and red open circles, respectively) versus the King model fits for globular-cluster-like objects in NGC 1052-DF2 observed in the *F*606*W* band. Δ is defined as

$$\Delta = (\chi^2_{\rm alternate} - \chi^2_{\rm K66})/(\chi^2_{\rm alternate} + \chi^2_{\rm K66}), \quad (5)$$

for comparing the χ^2 of the best fit of an alternative model with the χ^2 of the best fit of the King model (for details, see Barmby et al. 2007). It is evident that, if the value of Δ is zero, the two models fit the same sample object equally well. A positive value of Δ indicates

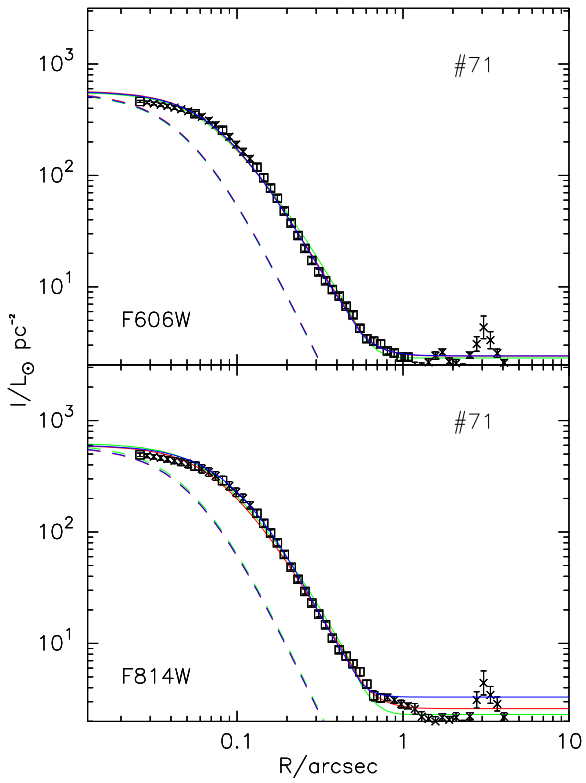

Figure 5. Same as Fig. 3, but with surface brightness profiles of and model fits to the sample object 71 in NGC 1052-DF2.

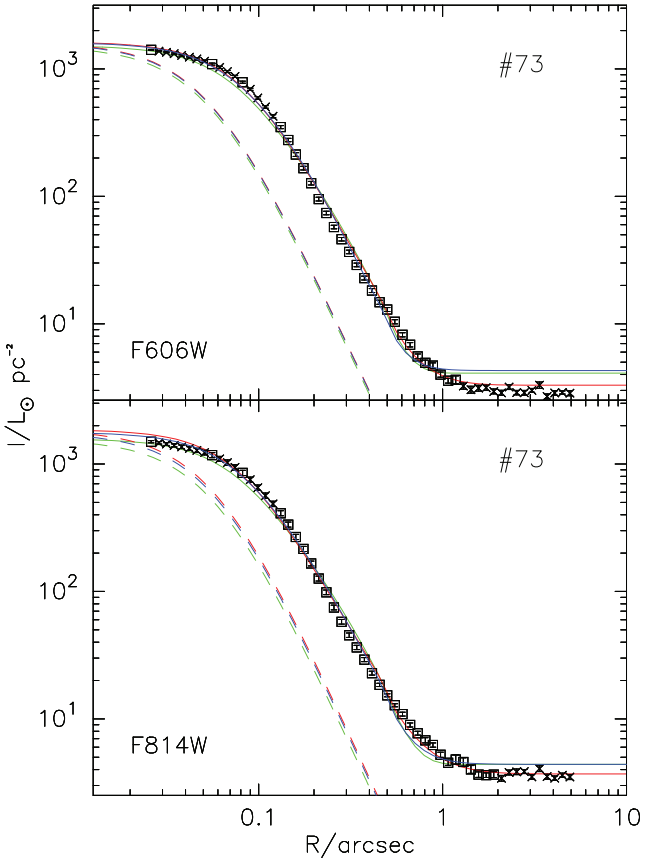

Figure 6. Same as Fig. 3, but with surface brightness profiles of and model fits to the sample object 73 in NGC 1052-DF2.

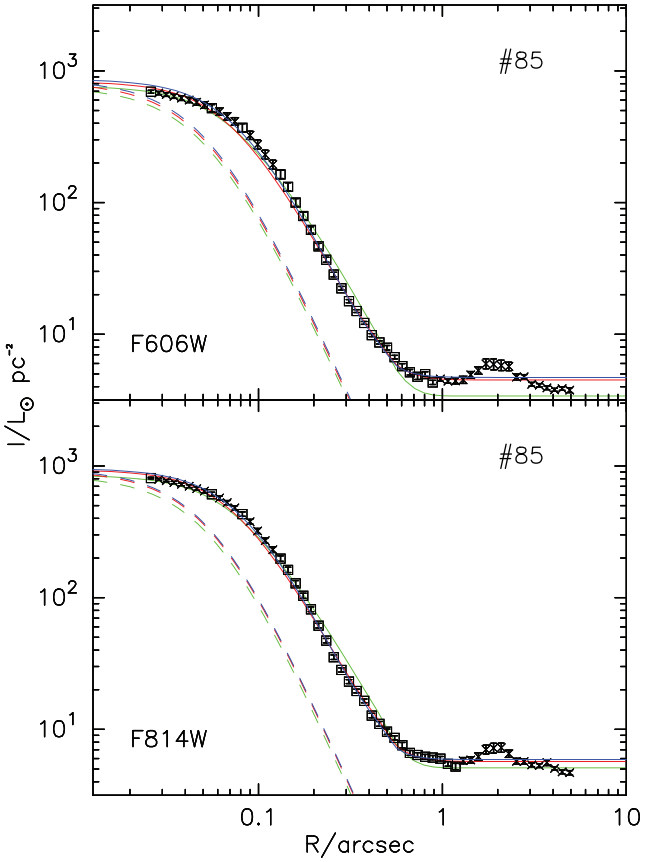

Figure 8. Same as Fig. 3, but with surface brightness profiles of and model fits to the sample object 85 in NGC 1052-DF2.

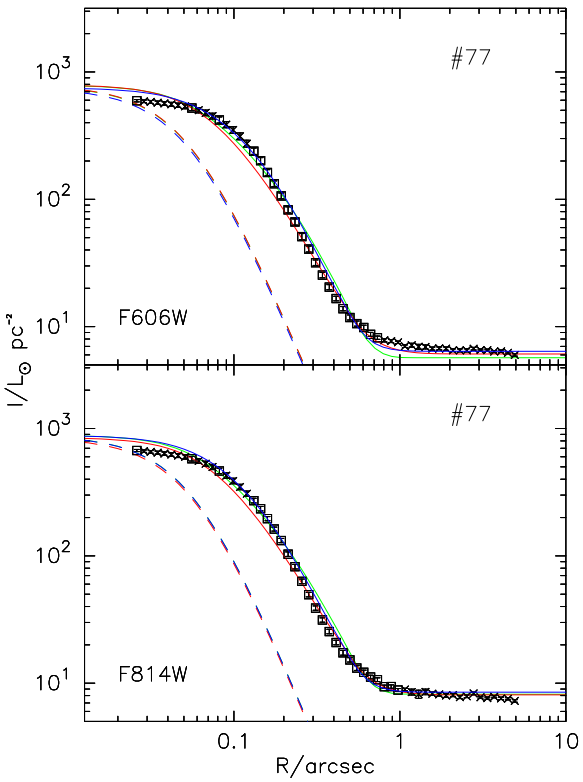

Figure 7. Same as Fig. 3, but with surface brightness profiles of and model fits to the sample object 77 in NGC 1052-DF2.

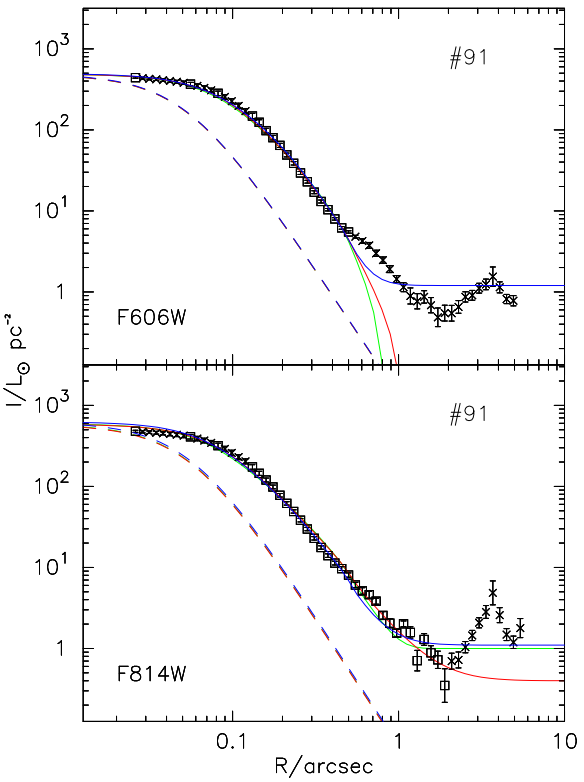

Figure 9. Same as Fig. 3, but with surface brightness profiles of and model fits to the sample object 91 in NGC 1052-DF2.

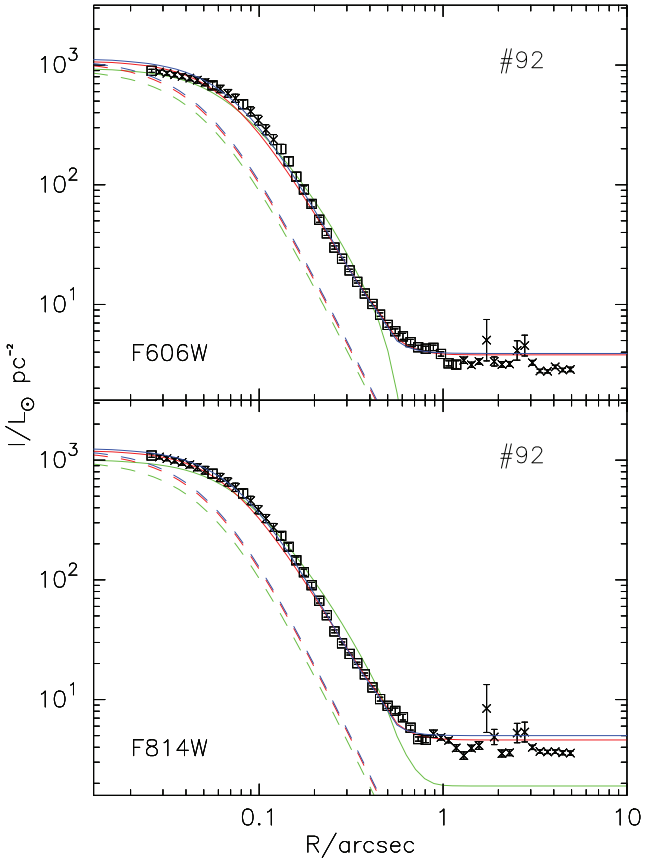

Figure 10. Same as Fig. 3, but with surface brightness profiles of and model fits to the sample object 92 in NGC 1052-DF2.

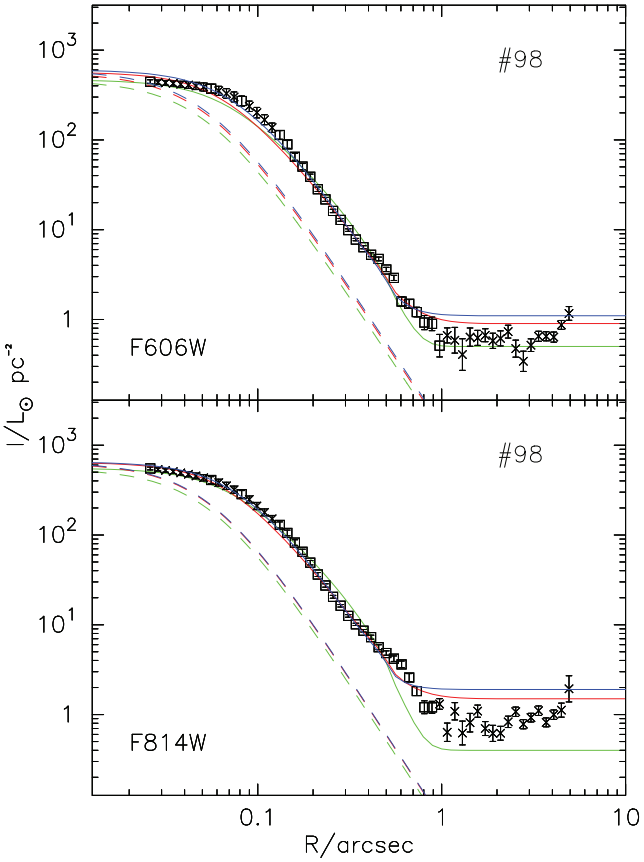

Figure 12. Same as Fig. 3, but with surface brightness profiles of and model fits to the sample object 98 in NGC 1052-DF2.

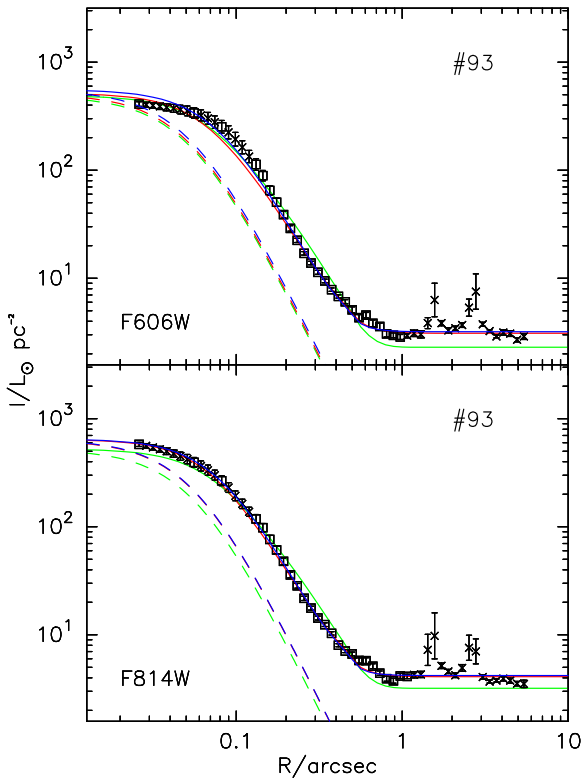

Figure 11. Same as Fig. 3, but with surface brightness profiles of and model fits to the sample object 93 in NGC 1052-DF2.

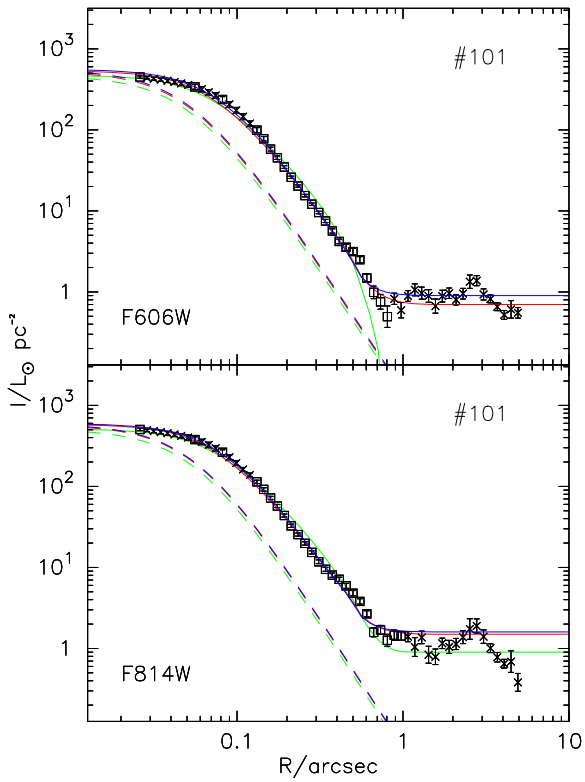

Figure 13. Same as Fig. 3, but with surface brightness profiles of and model fits to the sample object 101 in NGC 1052-DF2.

Table 5. Basic and structural parameters of the sample objects in NGC 1052-DF2. $N_{\rm pts}$ is the number of points in the intensity profile that were used for constraining the model fits. $\chi^2_{\rm min}$ is the minimum χ^2 obtained in the fits. $I_{\rm bkg}$ is the best-fitting background intensity. W_0 is the dimensionless central potential of the best fitting model, defined as $W_0 \equiv -\phi(0)/\sigma_0^2$. c/n is the concentration $c \equiv \log(r_{\rm t}/r_0)$. r_0 is the best-fitting model scale radius in parsec. $R_{\rm h}$ is the half-light, or effective radius of a model, which contains half the total object luminosity in projection, in units of parsec. $V_{\rm tot}$ is the total apparent V-band magnitude of a model object, defined as $V_{\rm tot} = 4.786 - 2.5\log(L_V/{\rm L}_\odot) + 5\log(D/10\ {\rm pc})$, where L_V is the V-band total integrated model luminosity, and it was obtained from the total integrated model luminosity in the $F606W$ and $F814W$ bands based on equations (6) and (7) of Barmby et al. (2007).

ID	Band	$N_{\rm pts}$	Model	$\chi^2_{\rm min}$	$I_{\rm bkg}$ ($L_\odot$ pc^{-2})	W_0	c/n	r_0 (pc)	$R_{\rm h}$ (pc)	$V_{\rm tot}$ (mag)
39	*F*606*W*	32	K66	4.29	0.30 ± 0.04	$7.90^{+0.73}_{-0.16}$	$1.80^{+0.22}_{-0.05}$	$1.724^{+0.048}_{-0.071}$	$14.128^{+0.557}_{-3.017}$	$22.45^{+0.05}_{-0.05}$
	...	32	W	1.16	0.10 ± 0.07	$6.70^{+0.11}_{-0.17}$	$2.17^{+0.07}_{-0.10}$	$3.066^{+0.045}_{-0.053}$	$14.536^{+1.202}_{-0.968}$	$22.35^{+0.05}_{-0.05}$
	...	32	S	2.74	0.30 ± 0.16	...	$2.55^{+0.04}_{-0.04}$	$0.061^{+0.001}_{-0.002}$	$13.917^{+1.251}_{-1.064}$	$22.40^{+0.06}_{-0.06}$
39	*F*814*W*	26	K66	3.66	0.40 ± 0.14	$7.30^{+0.32}_{-0.13}$	$1.62^{+0.09}_{-0.04}$	$2.436^{+0.105}_{-0.051}$	$14.371^{+1.659}_{-5.682}$	$22.49^{+0.08}_{-0.05}$
	...	26	W	1.38	0.20 ± 0.27	$6.10^{+0.22}_{-0.20}$	$1.84^{+0.11}_{-0.09}$	$3.860^{+0.048}_{-0.063}$	$14.324^{+1.729}_{-0.952}$	$22.35^{+0.05}_{-0.01}$
	...	26	S	1.95	0.50 ± 0.26	...	$2.15^{+0.04}_{-0.04}$	$0.193^{+0.004}_{-0.004}$	$14.129^{+1.152}_{-1.005}$	$22.39^{+0.05}_{-0.05}$
59	*F*606*W*	26	K66	3.53	1.30 ± 0.20	$8.10^{+0.54}_{-0.34}$	$1.86^{+0.17}_{-0.10}$	$1.370^{+0.065}_{-0.088}$	$13.501^{+1.232}_{-2.893}$	$22.95^{+0.05}_{-0.08}$
	...	26	W	2.15	0.60 ± 0.31	$7.60^{+0.33}_{-0.28}$	$2.86^{+0.24}_{-0.23}$	$1.724^{+0.066}_{-0.065}$	$17.035^{+6.398}_{-2.865}$	$22.65^{+0.07}_{-0.12}$
	...	26	S	2.21	1.40 ± 0.24	...	$3.05^{+0.04}_{-0.05}$	$0.011^{+0.001}_{-0.001}$	$13.008^{+2.396}_{-1.760}$	$22.92^{+0.17}_{-0.19}$
59	*F*814*W*	25	K66	8.27	2.60 ± 0.97	$8.10^{+0.99}_{-0.78}$	$1.86^{+0.30}_{-0.22}$	$1.370^{+0.085}_{-0.087}$	$14.142^{+0.693}_{-6.362}$	$22.88^{+0.10}_{-0.11}$
	...	25	W	3.44	3.00 ± 0.65	$10.70^{+0.64}_{-0.50}$	$3.37^{+0.07}_{-0.03}$	$0.097^{+0.005}_{-0.005}$	$13.573^{+1.661}_{-0.898}$	$22.65^{+0.18}_{-0.01}$
	...	25	S	3.09	3.30 ± 0.56	...	$2.80^{+0.05}_{-0.05}$	$0.022^{+0.001}_{-0.001}$	$12.925^{+2.140}_{-0.862}$	$22.96^{+0.15}_{-0.18}$
71	*F*606*W*	26	K66	5.45	2.30 ± 0.34	$8.60^{+0.99}_{-0.25}$	$2.01^{+0.30}_{-0.06}$	$0.970^{+0.059}_{-0.054}$	$13.782^{+1.496}_{-6.246}$	$22.78^{+0.08}_{-0.10}$
	...	26	W	2.61	2.40 ± 0.32	$10.80^{+0.53}_{-0.67}$	$3.37^{+0.06}_{-0.04}$	$0.097^{+0.004}_{-0.006}$	$13.117^{+1.244}_{-1.104}$	$22.79^{+0.18}_{-0.12}$
	...	26	S	2.21	2.40 ± 0.17	...	$3.05^{+0.03}_{-0.04}$	$0.011^{+0.001}_{-0.001}$	$13.008^{+2.396}_{-1.760}$	$22.65^{+0.17}_{-0.21}$
71	*F*814*W*	22	K66	4.95	2.30 ± 1.07	$8.10^{+1.27}_{-0.64}$	$1.86^{+0.39}_{-0.18}$	$1.370^{+0.062}_{-0.074}$	$14.142^{+0.791}_{-6.362}$	$22.74^{+0.08}_{-0.09}$
	...	22	W	1.87	2.60 ± 0.66	$10.90^{+0.56}_{-0.36}$	$3.38^{+0.06}_{-0.03}$	$0.097^{+0.004}_{-0.004}$	$13.940^{+1.294}_{-1.122}$	$22.79^{+0.18}_{-0.01}$
	...	22	S	1.63	3.30 ± 0.41	...	$1.85^{+0.06}_{-0.03}$	$0.386^{+0.015}_{-0.009}$	$12.954^{+2.072}_{-1.554}$	$22.17^{+0.05}_{-0.05}$
73	*F*606*W*	27	K66	23.39	4.10 ± 0.33	$7.60^{+0.58}_{-0.22}$	$1.71^{+0.17}_{-0.07}$	$1.935^{+0.112}_{-0.140}$	$13.443^{+1.080}_{-5.949}$	$21.65^{+0.06}_{-0.06}$
	...	27	W	13.30	3.30 ± 0.82	$6.70^{+0.36}_{-0.35}$	$2.17^{+0.26}_{-0.20}$	$2.733^{+0.110}_{-0.139}$	$13.668^{+3.430}_{-1.563}$	$21.55^{+0.05}_{-0.08}$
	...	27	S	14.47	4.30 ± 0.37	...	$2.30^{+0.05}_{-0.05}$	$0.109^{+0.007}_{-0.005}$	$12.635^{+2.232}_{-1.658}$	$21.65^{+0.06}_{-0.05}$
73	*F*814*W*	32	K66	18.76	4.40 ± 0.42	$7.90^{+1.29}_{-0.34}$	$1.80^{+0.39}_{-0.10}$	$1.724^{+0.094}_{-0.148}$	$14.763^{+1.393}_{-6.827}$	$21.66^{+0.08}_{-0.08}$
	...	32	W	8.42	3.70 ± 0.88	$7.20^{+0.42}_{-0.37}$	$2.53^{+0.35}_{-0.28}$	$1.935^{+0.076}_{-0.093}$	$14.958^{+5.421}_{-2.241}$	$21.56^{+0.06}_{-0.01}$
	...	32	S	11.58	4.40 ± 0.45	...	$3.10^{+0.04}_{-0.07}$	$0.010^{+0.000}_{-0.001}$	$13.963^{+2.555}_{-1.862}$	$21.65^{+0.18}_{-0.21}$
77	*F*606*W*	22	K66	22.28	5.70 ± 2.24	$11.10^{+1.84}_{-1.24}$	$2.57^{+0.39}_{-0.24}$	$0.273^{+0.024}_{-0.025}$	$16.571^{+2.181}_{-3.684}$	$22.02^{+0.11}_{-0.05}$
	...	22	W	10.72	6.10 ± 1.88	$12.00^{+0.45}_{-1.19}$	$3.52^{+0.08}_{-0.15}$	$0.097^{+0.009}_{-0.008}$	$15.990^{+1.796}_{-2.872}$	$22.14^{+0.24}_{-0.24}$
	...	22	S	11.53	6.40 ± 1.28	...	$1.70^{+0.09}_{-0.07}$	$0.864^{+0.040}_{-0.057}$	$15.518^{+4.948}_{-2.284}$	$21.95^{+0.05}_{-0.09}$
77	*F*814*W*	25	K66	26.02	8.20 ± 1.19	$10.80^{+1.93}_{-0.88}$	$2.51^{+0.44}_{-0.17}$	$0.307^{+0.020}_{-0.029}$	$16.796^{+2.366}_{-4.355}$	$22.04^{+0.11}_{-0.05}$
	...	25	W	11.80	8.10 ± 1.29	$12.00^{+0.48}_{-0.97}$	$3.52^{+0.08}_{-0.12}$	$0.097^{+0.009}_{-0.008}$	$16.634^{+1.802}_{-2.694}$	$22.14^{+0.22}_{-0.01}$
	...	25	S	14.09	8.50 ± 1.00	...	$1.85^{+0.10}_{-0.07}$	$0.545^{+0.032}_{-0.037}$	$15.598^{+4.774}_{-2.202}$	$21.75^{+0.05}_{-0.09}$
85	*F*606*W*	24	K66	31.16	3.40 ± 1.01	$8.10^{+1.05}_{-0.53}$	$1.86^{+0.32}_{-0.15}$	$1.370^{+0.090}_{-0.086}$	$13.501^{+0.734}_{-6.376}$	$22.45^{+0.09}_{-0.11}$
	...	24	W	2.97	4.50 ± 0.36	$9.90^{+0.19}_{-0.59}$	$3.33^{+0.01}_{-0.01}$	$0.097^{+0.002}_{-0.003}$	$11.771^{+0.376}_{-0.729}$	$22.59^{+0.10}_{-0.12}$
	...	24	S	2.91	4.70 ± 0.44	...	$2.85^{+0.04}_{-0.04}$	$0.015^{+0.001}_{-0.001}$	$11.339^{+0.808}_{-0.710}$	$22.51^{+0.09}_{-0.10}$
85	*F*814*W*	27	K66	23.71	5.10 ± 0.57	$8.10^{+1.02}_{-0.37}$	$1.86^{+0.31}_{-0.10}$	$1.370^{+0.077}_{-0.107}$	$14.142^{+0.693}_{-6.362}$	$22.41^{+0.09}_{-0.11}$
	...	27	W	3.89	5.70 ± 0.32	$9.90^{+0.33}_{-0.45}$	$3.33^{+0.01}_{-0.01}$	$0.097^{+0.004}_{-0.004}$	$12.417^{+0.532}_{-0.703}$	$22.59^{+0.15}_{-0.01}$
	...	27	S	3.34	5.90 ± 0.25	...	$2.70^{+0.04}_{-0.03}$	$0.024^{+0.001}_{-0.001}$	$11.853^{+0.817}_{-1.286}$	$22.39^{+0.15}_{-0.11}$
91	*F*606*W*	18	K66	7.24	-0.30 ± 0.39	$7.10^{+0.75}_{-0.14}$	$1.56^{+0.21}_{-0.04}$	$3.440^{+0.097}_{-0.159}$	$15.722^{+0.927}_{-1.984}$	$22.58^{+0.06}_{-0.06}$
	...	18	W	4.37	-0.30 ± 1.08	$6.50^{+0.59}_{-0.44}$	$2.05^{+0.40}_{-0.22}$	$4.331^{+0.089}_{-0.118}$	$16.491^{+5.007}_{-2.599}$	$22.56^{+0.05}_{-0.11}$
	...	18	S	5.38	1.20 ± 0.96	...	$1.75^{+0.05}_{-0.06}$	$0.686^{+0.029}_{-0.017}$	$14.641^{+2.770}_{-2.098}$	$22.94^{+0.05}_{-0.05}$
91	*F*814*W*	32	K66	8.19	1.00 ± 0.42	$8.20^{+1.73}_{-0.72}$	$1.89^{+0.52}_{-0.20}$	$1.935^{+0.131}_{-0.165}$	$17.822^{+1.387}_{-9.580}$	$22.49^{+0.12}_{-0.10}$
	...	32	W	5.51	0.40 ± 0.65	$7.50^{+0.81}_{-0.67}$	$2.77^{+0.46}_{-0.50}$	$3.066^{+0.123}_{-0.209}$	$23.073^{+30.029}_{-7.886}$	$22.56^{+0.16}_{-0.01}$
	...	32	S	6.02	1.10 ± 0.33	...	$3.20^{+0.08}_{-0.05}$	$0.010^{+0.001}_{-0.001}$	$16.518^{+3.505}_{-2.555}$	$24.00^{+0.26}_{-0.22}$
92	*F*606*W*	27	K66	30.11	-0.60 ± 3.49	$8.10^{+1.14}_{-0.77}$	$1.86^{+0.35}_{-0.22}$	$1.370^{+0.094}_{-0.092}$	$13.501^{+1.268}_{-6.376}$	$22.21^{+0.20}_{-0.09}$
	...	27	W	3.08	3.80 ± 0.28	$9.30^{+0.37}_{-0.18}$	$3.32^{+0.01}_{-0.01}$	$0.097^{+0.002}_{-0.003}$	$11.042^{+0.607}_{-0.245}$	$22.39^{+0.13}_{-0.09}$
	...	27	S	3.61	3.90 ± 0.25	...	$2.95^{+0.03}_{-0.03}$	$0.010^{+0.001}_{-0.001}$	$10.746^{+0.733}_{-0.608}$	$22.31^{+0.15}_{-0.09}$

Table 5 – *continued*

ID	Band	N_{pts}	Model	χ^2_{min}	I_{bkg} ($L_\odot$ pc^{-2})	W_0	c/n	r_0 (pc)	R_h (pc)	V_{tot} (mag)
92	*F814W*	23	K66	55.55	1.90 ± 2.24	$7.60^{+0.70}_{-0.63}$	$1.71^{+0.21}_{-0.19}$	$1.935^{+0.163}_{-0.160}$	$14.071^{+1.660}_{-5.977}$	$22.18^{+0.21}_{-0.13}$
	...	23	W	3.67	4.60 ± 0.61	$9.10^{+0.29}_{-0.46}$	$3.33^{+0.01}_{-0.01}$	$0.097^{+0.002}_{-0.003}$	$11.479^{+0.464}_{-0.560}$	$22.39^{+0.09}_{-0.01}$
	...	23	S	3.20	5.00 ± 0.44	...	$2.85^{+0.03}_{-0.03}$	$0.012^{+0.001}_{-0.001}$	$10.990^{+0.673}_{-0.557}$	$22.28^{+0.12}_{-0.09}$
93	*F606W*	25	K66	22.30	2.30 ± 0.66	$8.10^{+1.07}_{-0.88}$	$1.86^{+0.33}_{-0.26}$	$1.370^{+0.094}_{-0.099}$	$13.501^{+0.734}_{-2.893}$	$22.92^{+0.05}_{-0.12}$
	...	25	W	2.41	3.10 ± 0.21	$9.80^{+0.22}_{-0.23}$	$3.33^{+0.01}_{-0.01}$	$0.097^{+0.003}_{-0.004}$	$11.649^{+0.499}_{-0.732}$	$23.12^{+0.23}_{-0.17}$
	...	25	S	2.95	3.20 ± 0.20	...	$2.80^{+0.02}_{-0.05}$	$0.017^{+0.001}_{-0.001}$	$11.118^{+1.717}_{-1.247}$	$22.97^{+0.14}_{-0.21}$
93	*F814W*	26	K66	21.89	3.20 ± 0.73	$8.10^{+0.97}_{-0.57}$	$1.86^{+0.30}_{-0.16}$	$1.370^{+0.105}_{-0.099}$	$14.142^{+1.132}_{-6.362}$	$22.93^{+0.11}_{-0.11}$
	...	26	W	1.86	4.10 ± 0.26	$9.10^{+0.48}_{-0.56}$	$3.33^{+0.01}_{-0.01}$	$0.097^{+0.004}_{-0.004}$	$11.479^{+0.689}_{-0.560}$	$23.12^{+0.09}_{-0.01}$
	...	26	S	1.78	4.20 ± 0.22	...	$2.90^{+0.02}_{-0.04}$	$0.011^{+0.001}_{-0.001}$	$11.182^{+1.516}_{-0.592}$	$22.73^{+0.11}_{-0.16}$
98	*F606W*	25	K66	16.90	0.50 ± 0.66	$8.10^{+1.06}_{-0.80}$	$1.86^{+0.33}_{-0.23}$	$1.370^{+0.067}_{-0.092}$	$13.501^{+1.710}_{-2.893}$	$23.01^{+0.05}_{-0.06}$
	...	25	W	4.06	0.90 ± 0.31	$9.00^{+0.17}_{-0.34}$	$3.32^{+0.01}_{-0.01}$	$0.137^{+0.005}_{-0.006}$	$11.933^{+0.378}_{-1.116}$	$23.01^{+0.13}_{-0.16}$
	...	25	S	5.46	1.10 ± 0.25	...	$2.95^{+0.03}_{-0.04}$	$0.011^{+0.000}_{-0.001}$	$11.248^{+1.760}_{-1.278}$	$22.87^{+0.26}_{-0.17}$
98	*F814W*	24	K66	23.52	0.40 ± 1.02	$8.10^{+1.17}_{-0.48}$	$1.86^{+0.36}_{-0.14}$	$1.370^{+0.092}_{-0.110}$	$14.142^{+1.204}_{-6.362}$	$22.87^{+0.21}_{-0.09}$
	...	24	W	4.82	1.50 ± 0.54	$8.80^{+0.31}_{-0.38}$	$3.33^{+0.01}_{-0.05}$	$0.137^{+0.005}_{-0.005}$	$12.210^{+0.804}_{-1.234}$	$23.01^{+0.14}_{-0.01}$
	...	24	S	5.20	1.90 ± 0.41	...	$2.85^{+0.04}_{-0.04}$	$0.014^{+0.001}_{-0.001}$	$11.458^{+1.611}_{-1.177}$	$22.70^{+0.20}_{-0.16}$
101	*F606W*	23	K66	16.48	-0.10 ± 0.80	$8.10^{+0.67}_{-0.51}$	$1.86^{+0.21}_{-0.15}$	$1.370^{+0.085}_{-0.083}$	$13.501^{+1.680}_{-2.893}$	$22.96^{+0.10}_{-0.08}$
	...	23	W	2.68	0.70 ± 0.24	$9.80^{+0.18}_{-0.49}$	$3.33^{+0.01}_{-0.01}$	$0.097^{+0.002}_{-0.003}$	$11.649^{+0.499}_{-0.607}$	$23.06^{+0.09}_{-0.13}$
	...	23	S	3.02	0.90 ± 0.33	...	$2.80^{+0.04}_{-0.05}$	$0.017^{+0.001}_{-0.001}$	$11.118^{+0.789}_{-0.667}$	$22.97^{+0.09}_{-0.09}$
101	*F814W*	25	K66	11.69	0.90 ± 0.54	$8.10^{+0.88}_{-0.39}$	$1.86^{+0.27}_{-0.11}$	$1.370^{+0.092}_{-0.118}$	$14.142^{+1.132}_{-6.362}$	$22.96^{+0.23}_{-0.09}$
	...	25	W	3.22	1.50 ± 0.29	$9.70^{+0.45}_{-0.39}$	$3.32^{+0.02}_{-0.01}$	$0.097^{+0.003}_{-0.004}$	$12.168^{+0.782}_{-0.453}$	$23.06^{+0.13}_{-0.01}$
	...	25	S	3.30	1.60 ± 0.21	...	$2.95^{+0.03}_{-0.04}$	$0.011^{+0.001}_{-0.001}$	$11.879^{+1.755}_{-1.289}$	$22.78^{+0.20}_{-0.17}$

Table 6. 'Best-fitting' half-light radii and absolute magnitudes of the sample objects in NGC 1052-DF2.

ID	R_h (pc)	$M_{V,606}$ (mag)
39	$14.54^{+1.202}_{-0.968}$	$-9.23^{+0.05}_{-0.05}$
59	$17.04^{+6.398}_{-2.865}$	$-8.93^{+0.07}_{-0.12}$
71	$13.12^{+1.244}_{-1.104}$	$-8.79^{+0.18}_{-0.12}$
73	$13.67^{+3.430}_{-1.563}$	$-10.03^{+0.05}_{-0.08}$
77	$15.99^{+1.796}_{-2.872}$	$-9.44^{+0.24}_{-0.24}$
85	$11.77^{+0.376}_{-0.729}$	$-8.99^{+0.10}_{-0.12}$
91	$16.49^{+5.007}_{-2.599}$	$-9.02^{+0.05}_{-0.11}$
92	$11.04^{+0.607}_{-0.245}$	$-9.19^{+0.13}_{-0.09}$
93	$11.65^{+0.499}_{-0.732}$	$-8.46^{+0.23}_{-0.17}$
98	$11.93^{+0.378}_{-1.116}$	$-8.57^{+0.13}_{-0.16}$
101	$11.65^{+0.499}_{-0.607}$	$-8.52^{+0.09}_{-0.13}$

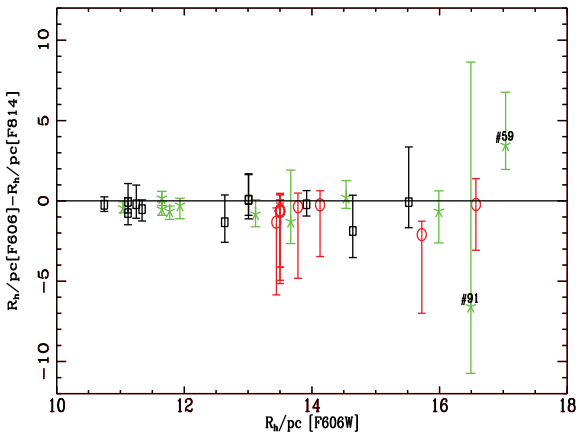

Figure 14. Comparison of half-light radius for model fits to the sample objects observed in both *F606W* and *F814W* bands: red open circles, King (1966) model; squares, Sérsic (1968) model; green stars, Wilson (1975) model.

a better fit of the King model, and a negative value implies that the alternative model is a better fit than the King model.

The Δ values are shown as a function of the Wilson model half-light radius in Fig. 15, which shows that nearly all the sample objects are better fitted by the Wilson model than by the King or Sérsic models. In addition, for all the sample objects, the Sérsic and Wilson models fit better than the King model. In the *F606W* band, there are two objects (71 and 85) that are better fitted by the Sérsic model than by the Wilson model, and $\Sigma\Delta = -5.25$ and $\Sigma\Delta = -4.94$ for the Wilson and Sérsic models, respectively. It is true that the Wilson model fits the sample objects marginally better than the Sérsic model. However, we selected the half-light radii obtained by the Wilson model fit as the final values of the sample objects, which are listed in Table 6. In fact, from Table 5, we can see that the half-light radii derived by fitting different models are not different. In order to present clearly the difference of half-light radius derived by fitting different models, Fig. 16 shows the relative differences of half-light radii for the King and Sérsic model fits (red open and filled circles, respectively) versus the Wilson model fit for the sample objects in NGC 1052-DF2 observed in the *F606W* band. The results show that, except for object 59, the values of half-light radius derived by fitting different models are consistent. For the six

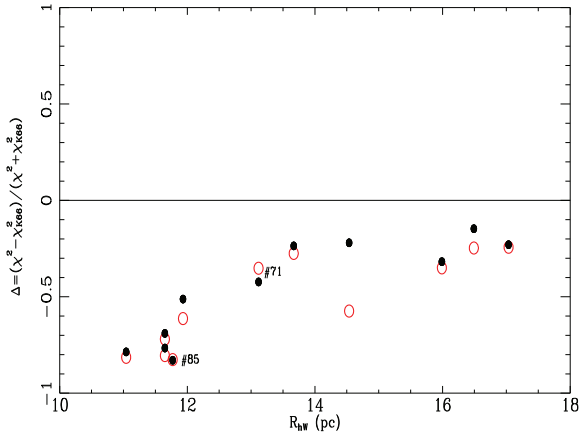

Figure 15. Comparison of goodness of sample object model fits as a function of the Wilson model half-light radius: filled circles, Wilson model; red open circles, Sérsic model.

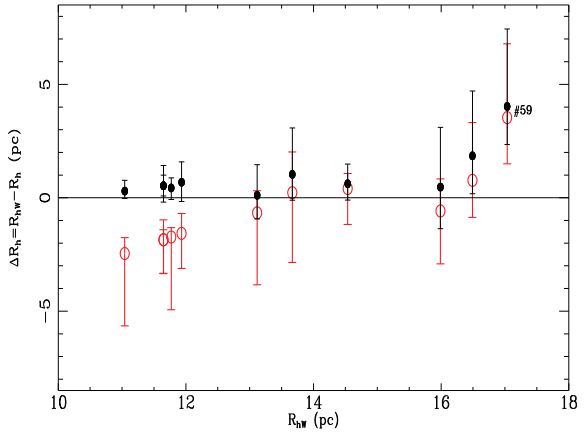

Figure 16. Comparison of half-light radius derived by fitting different models. Relative differences of half-light radii for the King (red open circles) and Sérsic (filled circles) model fits compared with the Wilson model fit for the sample objects in this paper.

objects, the half-light radii derived by fitting the King model are larger than those derived by fitting the Wilson model.

4 COMPARISON WITH PREVIOUS RESULTS AND DISCUSSION

Recently, van Dokkum et al. (2018a) derived the magnitudes, ellipticities and half-light radii for all 11 sample objects here using *HST* imaging, as used here. The magnitudes were obtained using SEXTRACTOR (Bertin & Arnouts 1996) in van Dokkum et al. (2018a). Then, they fitted King (1962) models to the surface brightness profiles using GALFIT software (Peng et al. 2002) with synthetic PSFs. The circularized half-light radii were determined from the measured core and tidal radii (multiplied by $\sqrt{b/a}$) based on eight independent measurements (four in V_{606} and four in I_{814}). The mean values of half-light radii are the biweight averages of the eight individual measurements. Trujillo et al. (2019) also derived the magnitudes, ellipticities and half-light radii for all these 11 sample objects here using *HST* imaging, as used here. As van Dokkum et al. (2018a) did, Trujillo et al. (2019) derived the magnitudes using SEXTRACTOR (Bertin & Arnouts 1996). In addition, Trujillo et al. (2019) derived ellipticities and the half-light radii for these sample

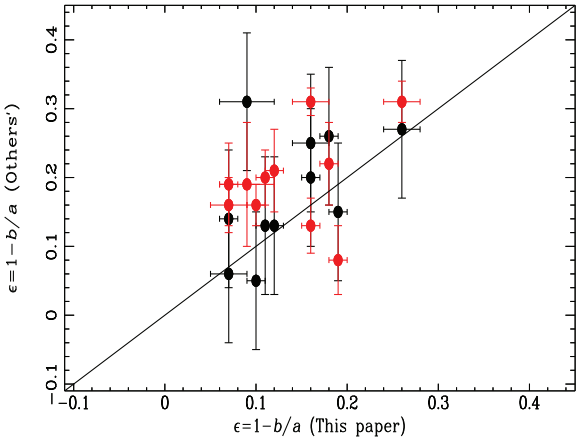

Figure 17. Comparison of our ellipticities of sample objects with previous results in van Dokkum et al. (2018a) and Trujillo et al. (2019). The black circles indicate the comparison between van Dokkum et al. (2018a) and us, and red filled circles indicate the comparison between Trujillo et al. (2019) and us. The solid line is a diagonal line.

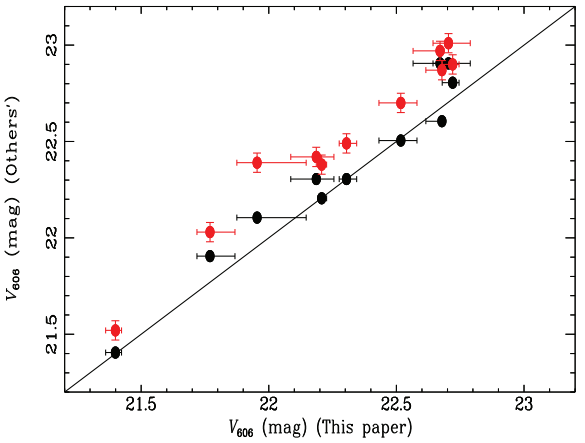

Figure 18. Comparison of our magnitudes of sample objects with previous results in van Dokkum et al. (2018a) and Trujillo et al. (2019). The black circles indicate the comparison between van Dokkum et al. (2018a) and us, and red filled circles indicate the comparison between Trujillo et al. (2019) and us. The solid line is a diagonal line.

objects using PSF-convolved King (1962) and Sérsic (1968) models. The model fittings of the sample objects were performed using IMFIT (Erwin 2015). Figs 17–19 show the comparisons between previous results (van Dokkum et al. 2018a; Trujillo et al. 2019) and our results. Fig. 17 shows that the ellipicities obtained here are in good agreement with those of van Dokkum et al. (2018a) and Trujillo et al. (2019), although there are some scatters. Fig. 18 shows that the magnitudes obtained here are in better agreement with those of van Dokkum et al. (2018a), although our results are also consistent with those of Trujillo et al. (2019). The offset of the differences between magnitudes of van Dokkum et al. (2018a) and ours is −0.077 mag, and the offset of the differences between magnitudes of Trujillo et al. (2019) and ours is −0.218 mag. In fact, Trujillo et al. (2019) found that the location of the peaks of the luminosity functions for these objects is in good agreement between Trujillo et al. (2019) and van Dokkum et al. (2018a). Fig. 19 shows that the half-light radii obtained by van Dokkum et al. (2018a) and Trujillo et al. (2019) are smaller than ours. The offset of the differences between the half-

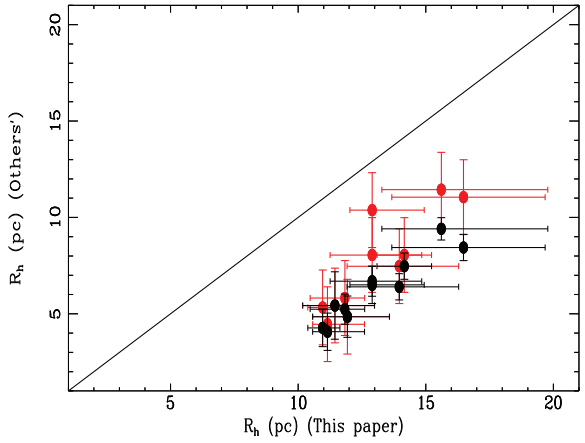

Figure 19. Comparison of our half-light radii of sample objects with previous results in van Dokkum et al. (2018a) and Trujillo et al. (2019). The black circles indicate the comparison between van Dokkum et al. (2018a) and us, and red circles indicate the comparison between Trujillo et al. (2019) and us. The solid line is a diagonal line.

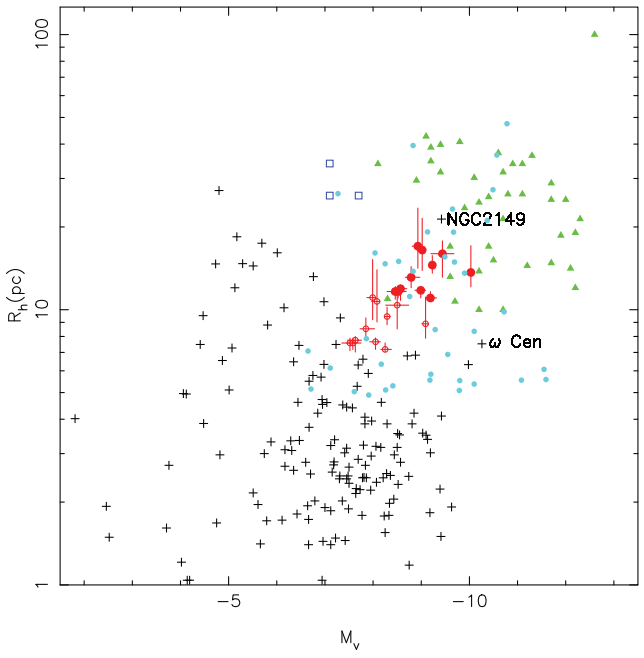

Figure 20. Half-light radii (R_h) versus absolute magnitudes (M_V) for the sample objects (filled red circles with error bars) in comparison with Galactic GCs from the on-line data base of Harris (1996) (2010 update) GCs (crosses). The green filled triangles are the confirmed UCDs from Brodie et al. (2011), the blue squares are the extended, luminous star clusters in the halo of M31 from Huxor et al. (2005), and the filled cyan circles are the extended star clusters (half-light radii greater than 5 pc) in NGC 4278, 4649 and 4697 from Forbes et al. (2013). The red circles are the sample objects in this paper, but the distance of $D = 13$ Mpc to NGC 1052-DF2 is used.

light radii of van Dokkum et al. (2018a) and ours is 6.17 pc, and the offset of the differences between the half-light radii of Trujillo et al. (2019) and ours is 4.99 pc. Our half-light radii are, on average, 11.74 pc, which corresponds to 53 and 43 per cent larger than those obtained by van Dokkum et al. (2018a) and Trujillo et al. (2019), respectively. In fact, the half-light radii obtained by van Dokkum et al. (2018a) are smaller than those obtained by Trujillo et al. (2019). Different methods used by the different groups may be the causes for the disagreement of half-light radii (Barmby, Holland & Huchra 2002).

The distribution of stellar systems in the luminosity versus half-light radius plane can provide interesting information on their evolutionary history. Using a plot of M_V versus $\log R_h$, van den Bergh & Mackey (2004) and Mackey & van den Bergh (2005) showed that three objects (ω Centauri, M54 and NGC 2419) in the Milky Way and G1 in M31 are seen to fall well above the sharp upper envelope of the main distribution of the GC clusters. Based on the position of a cluster on the size–luminosity plane, Mackey & van den Bergh (2005) suggested that the most luminous Local Group clusters, such as M54 and ω Centauri in the Milky Way, G1 in M31 and the most luminous clusters in NGC 2158, are the cores of former dwarf galaxies (also see Zinnecker et al. 1988; Freeman 1993; Meylan et al. 2001; Ma et al. 2007). Concerning the most luminous clusters in NGC 2158, Martini & Ho (2004) suggested that some of the massive GCs in NGC 2158 are nuclei of tidal dwarfs based on their large masses and the possible detection of extra-tidal light by Harris et al. (2002). Ever since the original work of Harris et al. (2002), there has been a large body of work that has shown that extra-tidal light around UCDs exists in real UCDs (see Evstigneeva et al. 2007; Liu et al. 2015; Voggel, Hilker & Richtler 2016; Wittmann et al. 2016; and references therein). However, stripped nuclei are very rare below stellar masses of 10^6 $M_\odot$ (Voggel et al. 2019). The only known ways to distinguish between GCs and stripped nuclei are based on massive black holes (see Seth et al. 2014; Ahn et al. 2017, 2018; Afanasiev et al. 2018; Voggel et al. 2018; and references therein), extended star formation history (Norris et al. 2015) or double component light profiles (see Strader et al. 2013; Liu et al. 2015; Voggel et al. 2016; Wittmann et al. 2016; and references therein).

Fig. 20 shows the half-light radius (R_h) versus absolute magnitude (M_V) diagram, where data for the 11 globular-cluster-like objects in NGC 1052-DF2 are plotted along with those for the Galactic GCs from the on-line data base of Harris (1996) (see the 2010 update), for the extended, luminous star clusters in the halo of M31 from Huxor et al. (2005), for the extended star clusters (half-light radii greater than 5 pc) in NGC 4278, 4649 and 4697 from Forbes et al. (2013), and for the UCDs from Brodie et al. (2011). In Fig. 20, we used the half-light radii of the sample objects obtained by fitting the radial surface brightness profiles in the $F606W$ band by the Wilson (1975) model (from Table 6). The absolute magnitude (M_V) (from Table 6) is corrected for foreground Galactic extinction, $E(B-V) = 0.024$, based on the dust map of Schlegel, Finkbeiner & Davis (1998). Fig. 20 makes it evident that all the sample objects occupy the same area of the UCDs from Brodie et al. (2011) and of the extended star clusters from Forbes et al. (2013), indicating that they are not normal GCs like those in the Milky Way. As mentioned in Section 1, there has been ongoing debate about the origin of UCDs. Mieske et al. (2013) proposed two UCD formation channels: one is a globular cluster channel, which is important mainly for UCDs with $M \lesssim 10^7$ $M_\odot$; another is tidal transformation of massive progenitor galaxies, which dominates for UCDs with $M \gtrsim 10^7$ $M_\odot$ and still contributes to lower UCD masses. Voggel et al. (2019) has estimated the occupation fraction of nuclei among UCDs based on integrated dynamical mass estimates that indicate the presence of a measurable central black hole. They find a small occupation fraction at low luminosities (< 20 per cent at $M_V < -10$), rising to ∼ 75 per cent at $M_V < -14.5$. Because the spectroscopically observed velocity dispersions of the sample objects here are not available, we cannot

derive their dynamical masses. It is true that these sample objects are more luminous than most normal Galactic GCs, and they have larger half-light radii than most normal Galactic GCs. So, we suggest that the globular-cluster-like objects in NGC 1052-DF2 studied here are not normal GCs like those in the Milky Way.

As mentioned in Section 1, Trujillo et al. (2019) argued in favour of the distance of $D = 13$ Mpc to NGC 1052-DF2. In Fig. 20, we also plot the half-light radius (R_h) versus absolute magnitude (M_V) diagram for the 11 globular-cluster-like objects in NGC 1052-DF2 using the distance of $D = 13$ Mpc to NGC 1052-DF2. Fig. 20 shows that these objects do not occupy the same area of the UCDs, and there are six objects that lie in the area of the normal GCs in the Milky Way.

5 SUMMARY

In this paper, we present the properties of the 11 globular-cluster-like objects in NGC 1052-DF2 using the *HST*/ACS/WFC images in the *F*606*W* and *F*814*W* bands. We derive their ellipticities, position angles and surface brightness profiles. Structural parameters are determined by fitting the profiles to three different models, including the King, Wilson and Sérsic models. Our results show that these objects are better fitted by the Wilson model than by the King and Sérsic models. The half-light radii obtained here are larger than those obtained by previous authors. The R_h versus M_V diagram shows that these globular-cluster-like objects occupy the same area of the UCDs and of the extended star clusters. Thus, we suggest that they are not normal GCs like those in the Milky Way.

ACKNOWLEDGEMENTS

We are indebted to the referee for thoughtful comments and insightful suggestions that improved this paper greatly. We would like to thank Dr McLaughlin for his help in finishing this paper. He provided us with a table including some parameters that were model-dependent functions of W_0 or c. This study has been supported by the National Key R&D Program of China No. 2019YFA0405501 and by the National Natural Science Foundation of China (NSFC; Nos. 11873053, 11603035, 11973042, 11890693 and 11890691).

REFERENCES

Afanasiev A. V. et al., 2018, MNRAS, 477, 4856
Ahn C. P. et al., 2017, ApJ, 839, 72
Ahn C. P. et al., 2018, ApJ, 858, 102
Amorisco N. C., Loeb A., 2016, MNRAS, 459, L51
Amorisco N. C., Monachesi A., White S. D. M., 2018, MNRAS, 475, 4235
Baes M., Gentile G., 2011, A&A, 525, A136
Barmby P., Holland S., Huchra J., 2002, AJ, 123, 1937
Barmby P., McLaughlin D. E., Harris W. E., Harris G. L. H., Forbe D. A., 2007, AJ, 133, 2764
Barmby P. et al., 2009, AJ, 138, 1667
Bertin E., Arnouts S., 1996, A&AS, 117, 393
Blakeslee J. P., Cantiello M., 2018, Research Notes of the American Astronomical Society, 2, 146
Brodie J. P., Romanowsky A. J., Strader J., Forbes D. A., 2011, AJ, 142, 199
Carleton T., Errani R., Cooper M., Kaplinghat M., Peñarrubia J., Guo Y., 2019, MNRAS, 485, 382
Chan T. K., Kereš D., Wetzel A., Hopkins P. F., Faucher-Giguère C.-A., El-Badry K., Garrison-Kimmel S., Boylan-Kolchin M., 2018, MNRAS, 478, 906
Drinkwater M. J., Jones J. B., Gregg M. D., Phillipps S., 2000, PASA, 17, 227
Erwin P., 2015, ApJ, 799, 226
Evstigneeva E. A., Drinkwater M. J., Jurek R., Firth P., Jones J. B., Gregg M. D., Phillipps S., 2007, MNRAS, 378, 1036
Forbes D. A., Pota V., Usher C., Strader J., Romanowsky A. J., Brodie J. P., Arnold J. A., Spitler L. R., 2013, MNRAS, 435, L6
Fosbury R. A. E., Mebold U., Goss W. M., Dopita M. A., 1978, MNRAS, 183, 549
Freeman K. C., 1993, in Dejonghe H., Habing H. J., eds, Galactic Bulges. Kluwer, Dordrecht, p. 263
Harris W. E., 1996, AJ, 112, 1487
Harris W. E., Harris G. L. H., Holland S. T., McLaughlin D. E., 2002, AJ, 124, 1435
He M., Wu H., Du W., Wicker J., Zhao P., Lei F., Liu J., 2019, ApJ, 880, 30
Hilker M., Infante L., Richtler T., 1999, A&AS, 138, 55
Huxor A. P., Tanvir N. R., Irwin M. J., Ibata R., Collett J. L., Ferguson A. M. N., Bridges T., Lewis G. F., 2005, MNRAS, 360, 1007
Karachentsev I. D., Karachentseva V. E., Suchkov A. A., Grebel E. K., 2000, A&AS, 145, 415
King I. R., 1962, AJ, 67, 471
King I. R., 1966, AJ, 71, 64
Lee J. H., Kang J., Lee M. G., Jang I. S., 2020, ApJ, 894, 75
Liao S. et al., 2019, MNRAS, 490, 5182
Lim S., Peng E. W., Côté P., Sales L. V., den Brok M., Blakeslee J. P., Guhathakurta P., 2018, ApJ, 862, 82
Liu C-Z. et al., 2015, ApJ, 812, L2
Ma J., 2015, AJ, 149, 157
Ma J. et al., 2007, MNRAS, 376, 1621
Ma J. et al., 2017, MNRAS, 468, 4513
Mackey A., van den Bergh S., 2005, MNRAS, 360, 631
McLaughlin D. E., van der Marel R. P., 2005, ApJS, 161, 304
McLaughlin D. E., Barmby P., Harris W. E., Forbes D. A., Harris G. L. H., 2008, MNRAS, 384, 563
Martini P., Ho L. C., 2004, ApJ, 610, 233
Meylan G., Sarajedini A., Jablonka P., Djorgovski S., Bridges T., Rich R., 2001, AJ, 122, 830
Michie R. W., 1963, MNRAS, 125, 127
Mieske S., Frank M. J., Baumgardt H., Lützgendorf N., Neumayer N., Hilker M., 2013, A&A, 558, A14
Norris M. A., Escudero C. G., Faifer F. R., Kannappan S. J., Forte J. C., van den Bosch R. C. E., 2015, MNRAS, 451, 3615
Noyola E., Gebhardt K., 2006, AJ, 132, 447
Pandya V. et al., 2018, ApJ, 858, 29
Peng C. Y., Ho L. C., Impey C. D., Rix H.-W., 2002, AJ, 124, 266
Rejkuba M., 2012, Ap&SS, 341, 195
Rhodes J. D., Massey R., Albert J., Taylor J. E., Koekemoer A. M., Leauthaud A., 2006, in Koekemoer A. M., Goudfrooij P., Dressel L. L., eds, The 2005 HST Calibration Workshop: Hubble After the Transition to Two-Gyro Mode. NASA, Greenbelt, p. 21
Schlegel D. J., Finkbeiner D. P., Davis M., 1998, ApJ, 500, 525
Sérsic J. L., 1968, Atlas de Galaxias Australes. Obs. Astronomico, Cordoba
Seth A. C. et al., 2014, Nature, 513, 398
Spekkens K., Karunakaran A., 2018, ApJ, 855, 28
Strader J. et al., 2013, ApJ, 775, L6
Tanvir N. R. et al., 2012, MNRAS, 422, 162
Toloba E. et al., 2018, ApJ, 856, L31
Trujillo I. et al., 2019, MNRAS, 486, 1192
van den Bergh S., Mackey A. D., 2004, MNRAS, 354, 713
van Dokkum P., Abraham R., Merritt A., Zhang J., Geha M., Conroy C., 2015a, ApJ, 798, L45
van Dokkum P. et al., 2015b, ApJ, 804, L26
van Dokkum P. et al., 2016, ApJ, 828, L6
van Dokkum P. et al., 2018a, ApJ, 856, L30
van Dokkum P., Danieli S., Cohen Y., Romanowsky A. J., Conroy C., 2018b, ApJ, 864, L18
van Dokkum P. et al., 2018c, Nature, 555, 629

Voggel K., Hilker M., Richtler T., 2016, A&A, 586, A102
Voggel K. T. et al., 2018, ApJ, 858, 20
Voggel K. T., Seth A. C., Baumgardt H., Mieske S., Pfeffer J., Rasskazov A., 2019, ApJ, 871, 159
Wang S., Ma J., 2013, AJ, 146, 20
White R. E., Shawl S. J., 1987, ApJ, 317, 246
Wilson C. P., 1975, AJ, 80, 175
Wittmann C., Lisker T., Pasquali A., Hilker M., Grebel E. K., 2016, MNRAS, 459, 4450
Zinnecker H., Keable C. J., Dunlop J. S., Cannon R. D., Griffiths W. K., 1988, in Proc. IAU Symp. 126, The Harlow-Shapley Symposium on Globular Cluster Systems in Galaxies. Kluwer, Dordrecht, p. 603

SUPPORTING INFORMATION

Supplementary data are available at *MNRAS* online.

Table S3. Intensity profiles for the sample objects in NGC 1052-DF2.

Please note: Oxford University Press is not responsible for the content or functionality of any supporting materials supplied by the authors. Any queries (other than missing material) should be directed to the corresponding author for the article.

This paper has been typeset from a TEX/LATEX file prepared by the author.